

Lowland river sinuosity on Earth and Mars set by the pace of meandering and avulsion

Received: 25 May 2022

Accepted: 23 June 2023

Published online: 03 August 2023

 Check for updates

Chenliang Wu¹, Wonsuck Kim¹✉, Ryan Herring¹, Benjamin T. Cardenas², Tian Y. Dong³, Hongbo Ma^{4,5,6}, Andrew Moodie⁷, Jeffrey A. Nittrouer⁸, Frank Tsai⁹ & An Li⁹

Meandering rivers have shaped the landscapes of Earth and Mars through the development of sinuous and migrating channels. River channel sinuosity reflects an interplay of primary agents including water discharge and sediment supply, information that is archived in the sedimentary record. Here we examine the spatial variability of the sinuosity of 21 lowland rivers on Earth and six ancient river systems on Mars using satellite imagery, and identify a dichotomy in spatial patterns: instead of decreasing downstream as previously suggested, we find that the sinuosity either increases or remains constant approaching the river outlet. We conduct numerical modelling of channel migration to show that these bimodal patterns can be explained as a competition between the timescale required for channels to establish steady-state sinuosity and the avulsion timescale. This highlights the role of varying water discharge on meander development and demonstrates how the planform morphology of modern and ancient fluvial systems may be used to interpret hydrological regimes of river systems, with implications for lowland river migration patterns under future shifting climate regimes.

Lowland rivers are a critical link in the continental hydrological cycle and are important conduits for water, sediment and nutrient fluxes. One of the most striking features of river channels is their self-formed sinuous patterns. The degree of sinuosity represents a fundamental aspect of planform morphology, and may be used to evaluate channel dynamics, including the rate of migration^{1,2}, and interpret the hydrological activities of rivers on Earth as well as on extraterrestrial planets³. Although previous studies have established first-order empirical relationships between fluvial properties (for example, discharge, drainage basin size^{3–6}, sediment supply⁷ and riverbank vegetation⁸) and river morphology (for example, meander wavelength, flow depth, sinuosity and channel migration rate),

uncertainty surrounding these relations precludes the interpretation of fluvial properties from planform morphology alone. This shortcoming limits the ability of empirical relations to predict river responses to environmental changes, as well as to estimate the palaeohydraulic conditions from the morphology expressed in the sedimentary record; for example, unravelling the duration of the Martian hydrological cycle that potentially provided the essential conditions for the development of life^{9,10}.

Previous research has demonstrated that, for coastal rivers, the sinuosity (Ω) typically decreases downstream nearing the outlet^{11,12}. This observation is consistent for modern systems on Earth (Fig. 1a,e; Extended Data Fig. 1) and for ancient Martian deltaic deposits^{13,14}

¹Department of Earth System Sciences, Yonsei University, Seoul, Republic of Korea. ²Department of Geosciences, The Pennsylvania State University, University Park, PA, USA. ³School of Earth, Environmental, and Marine Sciences, University of Texas Rio Grande Valley, Edinburg, TX, USA. ⁴State Key Laboratory of Hydrosience and Engineering, Tsinghua University, Beijing, China. ⁵Key Laboratory of Hydrosience of the Ministry of Water Resources, Tsinghua University, Beijing, China. ⁶Department of Hydraulic Engineering, Tsinghua University, Beijing, China. ⁷Department of Civil, Architectural and Environmental Engineering, University of Texas, Austin, TX, USA. ⁸Department of Geosciences, Texas Tech University, Lubbock, TX, USA. ⁹Department of Civil and Environmental Engineering, Louisiana State University, Baton Rouge, LA, USA. ✉e-mail: delta@yonsei.ac.kr

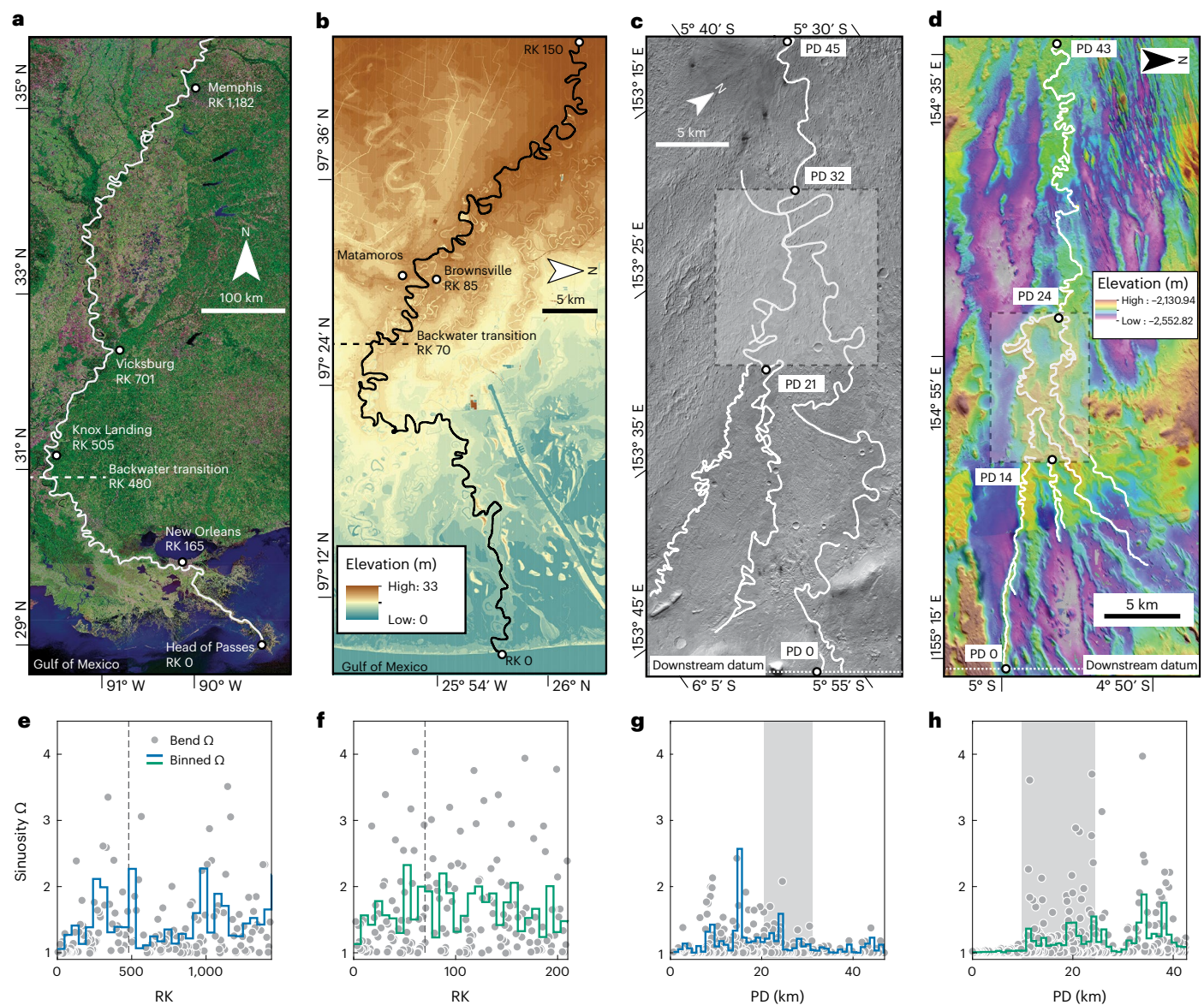


Fig. 1 Maps of meandering rivers and fluvial ridges and associated spatial variability in sinuosity. **a–d**, Mississippi River (**a**), Rio Grande (**b**) and two ancient deltaic channels in Aeolis Dorsa, Mars (**c,d**). **e–h**, Bend sinuosity (filled grey symbols) and binned average sinuosity (green and blue stairs) of the Mississippi River in **a** (**e**), the Rio Grande in **b** (**f**) and the Martian deltaic channels in **c** (**g**) and **d** (**h**). In **a–d**, the general flow direction is from top to bottom. In **c** and **d**, the datum (white dashed line) crosses the downstream-most location of the

ancient channel and is perpendicular to the down-dip direction. The avulsion nodes approximated by the backwater transitions (Methods) are noted by the dashed lines in **a** and **b** and **e** and **f**; the grey shaded boxes in **c** and **d** and **g** and **h** mark the avulsion locations. Credit: **a**, USGS under a Creative Commons licence [CC01.0](https://creativecommons.org/licenses/by/4.0/); **b**, US-side data from TNRS under a Creative Commons licence [CC01.0](https://creativecommons.org/licenses/by/4.0/), Mexico-side data from INEGI; **c,d**, Malin Space Science Systems and Caltech-JPL.

(Fig. 1c,g). Nevertheless, spatial variability in sinuosity for channels near the outlet has not been explored in previous studies^{3–5,7,8}, particularly in a temporal context. Here we explore the hypothesis that the timespan of an active channel, that is, the timescale of flow conveyance before abandonment via avulsion^{15–17}, and the rate of migration of a channel interact to establish the sinuosity of lowland rivers. We present the application of a numerical model that explains the spatial sinuosity patterns of lowland rivers and highlights the variability in water discharge as a first-order control on the channel migration rate. Our findings are directly applicable to quantitatively analysing the palaeohydrology of ancient systems from sedimentary records, and may also be leveraged to predict the migration dynamics of natural rivers in response to environmental stresses.

Spatial variability in river sinuosity

We target 21 large meandering lowland rivers on Earth and assess the sinuosity patterns extending from the avulsion node^{15,16,18} to the channel outlet at the coastal interface. The length of this stretch of river defines the avulsion length scale L_a . A group of 13 rivers (Mississippi, Nile, Trinity, Danube, Rhine, Meuse, Don, Kobuk, Yana, Mackenzie, Tombigbee, Alabama and Apalachicola) demonstrates that the average sinuosity increases substantially around the avulsion node but decreases drastically with progression downstream towards the river outlet (Figs. 1a and 2a; Extended Data Fig. 1). The sinuosity averaged over L_a is 1.22–1.25 upstream of the avulsion node ($RK/L_a > 1$, where RK denotes the river kilometre, the along-stream distance with respect to the channel outlet) but increases to 1.36 downstream of the deltaic avulsion node ($0 < RK/L_a < 1$). The reach-averaged sinuosity with a reach

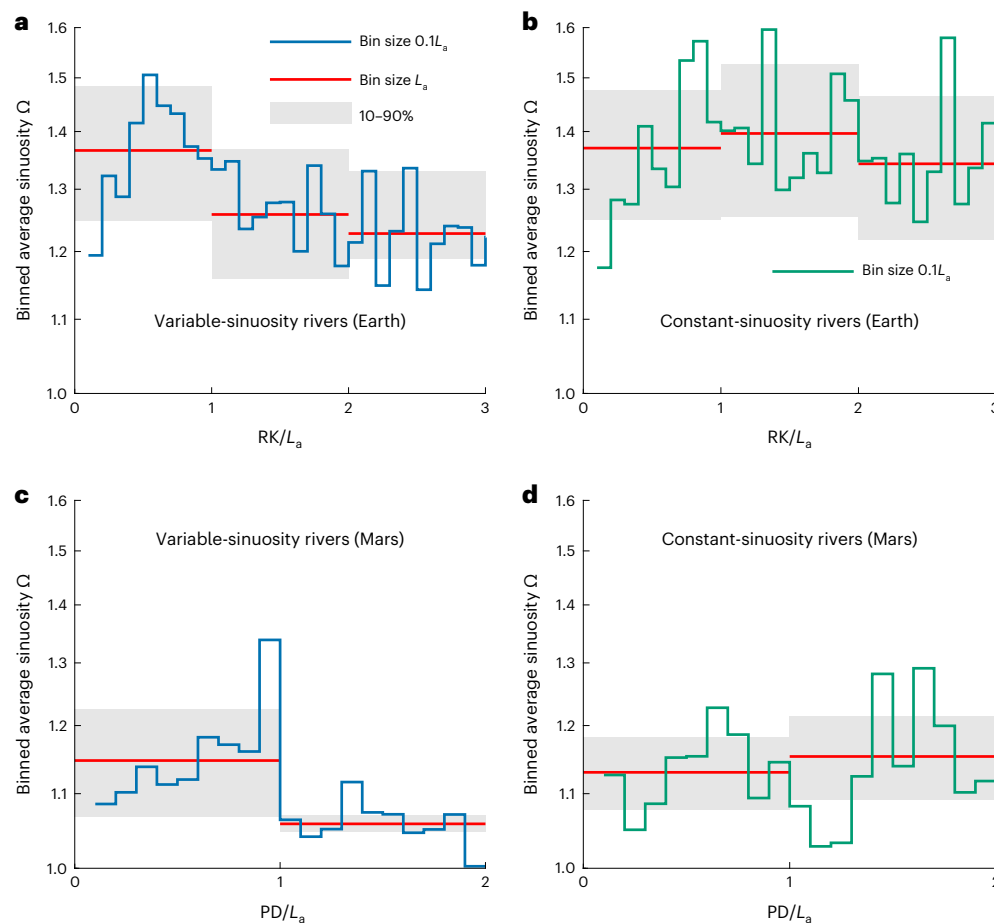


Fig. 2 | Spatial variability in the binned average sinuosity. a, Variable-sinuosity rivers on Earth. **b**, Constant-sinuosity rivers on Earth. **c**, Variable-sinuosity rivers on Mars. **d**, Constant-sinuosity rivers on Mars. The abscissa (that is, RK (**a,b**) and

PD (**c,d**)) is normalized by each avulsion length (L_a) (see Methods). Bin sizes are $0.1L_a$ for the blue and green lines, and L_a for the red lines; the grey shaded boxes mark the 10–90 percentile range of the bootstrapped average sinuosity.

scale of $0.1L_a$ peaks at a value of 1.5 ($RK/L_a = 0.5$) and then decreases to around 1.20 closer the outlet ($RK/L_a = 0$) (Fig. 2a). Alternatively, a second group of eight rivers (Brazos, Rio Grande, Colorado, Indus, Chao Phraya, Sabine, Neches and Suwannee) demonstrates a consistent sinuosity of around 1.34–1.40 when averaged over L_a , albeit maintaining local variability, without any spatial relation to the avulsion node (Figs. 1b and 2b; Extended Data Fig. 2). Therefore, we refer to these two groups of rivers as ‘variable-sinuosity rivers’ and ‘constant-sinuosity rivers’, respectively. A Mann–Kendall statistical test, based on the reach-averaged sinuosity, rejects the null hypothesis that the sinuosity is independently distributed without a monotonic trend for the variable-sinuosity rivers at the 5% significance level ($P = 7 \times 10^{-4}$); the same test fails to reject the null hypothesis for the constant-sinuosity rivers ($P = 0.8864$).

The sinuosity of ancient Martian deltaic channels, measured using fluvial ridge centrelines^{19–21} (Methods), is determined from six well-studied ancient rivers at Aeolis Dorsa^{13,14,22} (Fig. 1c,d). The platform channel morphology provides a means to approximate the location of deltaic avulsions for the Martian river systems²³. For example, the downstream channel network converges to form fewer channels with progression upstream within a narrow reach (Fig. 1c,d). This suggests the existence of deltaic-lobe avulsion nodes near this region^{15,17,24,25}, particularly given the proximity of these river systems to their associated contemporaneous palaeoshorelines^{13,14,22}. These six Martian systems also show the dichotomy in the sinuosity patterns found in the Earth rivers (Fig. 2c,d; Extended Data Fig. 3). For the first group of three Martian river systems, bends downstream of the avulsion locations are

characterized by high sinuosity (>2), and the sinuosity averaged over L_a increases downstream from 1.06 to 1.15 across the avulsion node (Figs. 1g and 2c; Extended Data Fig. 3a–f). The reach-averaged sinuosity with a reach scale of $0.1L_a$ shows a distinct peak of 1.34 ($PD/L_a = 0.9$, where PD denotes the projected distance from the channel bend to the downstream distal reach of the fluvial sandstone ridges) downstream of the avulsion node (that is, for $PD/L_a = 1$). For the second group of three Martian river systems, the average sinuosity fluctuates around 1.13–1.16; unlike the first group, there is no distinct increase in sinuosity around the avulsion nodes (Fig. 1h; Extended Data Fig. 3g–i). A Mann–Kendall statistical test supports the interpretations of variable ($P = 0.02$) and constant ($P = 0.39$) sinuosity for these first and second groups of Martian rivers, respectively. Overall, the Martian and Earth river systems are comparable, but the averaged sinuosity is generally lower for the Martian rivers compared with the Earth rivers, which is due to the integration of multiple channel paths, potentially over a range of different ages, for Mars^{13,22} (Extended Data Fig. 3). In fact, some Martian river systems developed high-sinuosity bends that are indistinguishable from Earth rivers (Extended Data Fig. 3).

Sinuosity development through the avulsion cycle

Rivers near the outlet typically possess a super-elevated avulsion node^{18,23,24}. The channel sinuosity typically evolves towards a steady state²⁶ until an avulsion resets the sinuosity and initiates a subsequent cycle of the channel development^{15,17}. Numerical simulations of the

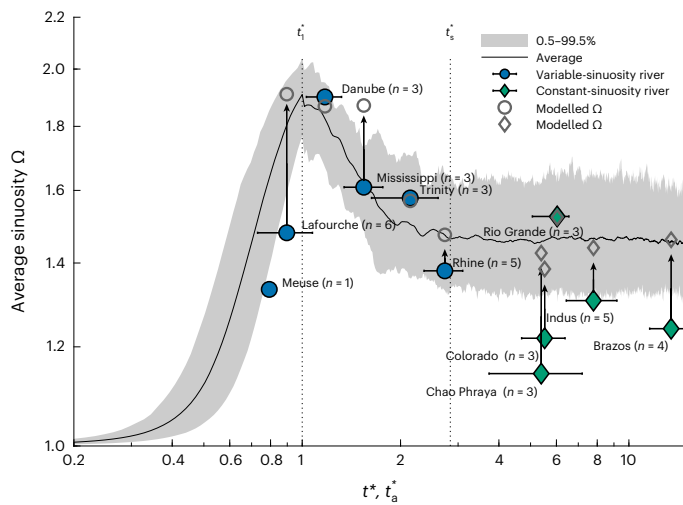


Fig. 3 | Measured river sinuosity compared to model results. Modelled temporal variabilities in the channel sinuosity and normalized age t_a^* ($t_a^* = t_a/t_1$) of the lowermost reach (downstream of the avulsion node) for the variable- and constant-sinuosity rivers (filled blue and green symbols, respectively, with error bars). Open circles and diamonds represent the modelled channel sinuosities for natural rivers with neck cutoffs only. The arrows mark the difference between the measured and modelled sinuosities for natural rivers. The error bars denote the maximum and minimum of the normalized age t_a^* of natural rivers calculated based on values of the calibrated erosional coefficient E (where n denotes the number of E estimates (Supplementary Information)). The grey shaded area marks the range of the 0.5–99.5 percentile range of the modelled average sinuosity from 1,000 simulations of rivers (Supplementary Information). The associated average across all the simulations is represented by the black line. The slope of the fitted linear regression function between the sinuosity and the normalized time t^* ($t^* = t/t_1$) is evaluated from t_1^* ($t_1^* = t_1/t_1$) to the upper end of the time domain. The value of the normalized time to reach the steady state t_s^* ($t_s^* = t_s/t_1$) is established where the slope of the linear regression function approaches a value of zero. For the variable-sinuosity rivers (blue symbols), the average sinuosity is measured for channel reaches within the upper one-third of the channel reach downstream of the avulsion node, assuming that age can be approximated by the observed avulsion time. The channel within this reach becomes younger progressing downstream as the river mouth progrades through time during an avulsion cycle. Thus, the lower reaches are excluded in the analysis as ages cannot be specified. See Extended Data Figs. 4–6 and Supplementary Table 1 for data used from each river.

development of the meandering river planform were carried out using different channel sizes and bed slopes (Supplementary Information) to establish that, over time (t), the average sinuosity increases and reaches a maximum before decreasing to a steady-state value (Fig. 3). Two key development timescales emerge: the time taken to reach the maximum average sinuosity (t_1), which marks the time before the development of meander neck cutoffs; and the time taken to achieve an average sinuosity after establishing the steady state (t_s). Our model simulations suggest that, given sufficient time (that is, t_s), the average sinuosity fluctuates around a mean value^{7,26}.

We hypothesize that the pace of meander development and the avulsion frequency determine the sinuosity pattern of a channel from the avulsion node to the river outlet^{15,16,18,23}. Specifically, a fast-migrating channel can reach the steady state before an avulsion event so that the entirety of the river reach downstream of the avulsion node establishes a consistent sinuosity (for example, Figs. 1b,f and 2b). Alternatively, if an avulsion event happens before t_s for a slowly migrating channel, the sinuosity downstream of the avulsion node can have a value which is greater than that from the upstream reach of the avulsion node; in such a case, distinct peaks emerge in the sinuosity spatial trends (for example, Figs. 1a,e and 2a).

To test this hypothesis, for several lowland river systems we compared the age of a river near its avulsion node (t_a , the time since the last avulsion to the present date) with that of the modelled t_1 and t_s data (Supplementary Information; Extended Data Table 1). For the variable-sinuosity rivers, t_a pre-dates t_s so that the current river courses have yet to reach a steady state with respect to the average channel sinuosity (Fig. 3). The modelled average sinuosity shows good agreement with the measured average sinuosity. For the constant-sinuosity rivers, t_a is close to or greater than t_s such that all analysed systems have achieved steady-state conditions. Hence, the average sinuosity shows no substantial increase or decrease, and is lower compared with the modelled peak average sinuosity around t_1 (Fig. 3). Compared with the model output, the lower sinuosity values measured for the natural rivers could be due to processes occurring in natural systems that are not represented in the model framework, such as chute cutoffs, which prevent higher sinuosity²⁷. Evidence for this is also provided by the simulation results for natural river systems when considering neck cutoffs only, where the data show better fits to the predicted sinuosity trends which are generally greater than the measured sinuosity values (open circles and diamonds in Fig. 3).

Physical controls on the channel migration rate

The distinction in spatial trends of the channel sinuosity between the two river groups reflects differences in the channel migration rates and avulsion timescales. The avulsion timescales for the rivers range from centuries to millennia (values that are typical for lowland rivers¹⁵) and are within just a factor of three (Supplementary Information; Extended Data Table 1). By contrast, the normalized channel migration rate r^* (Methods) maintains a much higher difference between the two groups—up to an order of magnitude—despite the river channels encompassing bed slopes within a factor of four (between 2×10^{-4} and 5×10^{-5}). The channel migration rate normalized to the channel width and the exceedance probability of bankfull discharge (Methods) provides a means to compare the associated impact on the channel planform morphology across various river sizes²⁸. Although a previous study suggested that the channel migration rate increases with the river size⁸, our analysis demonstrates that small rivers can possess a much higher normalized migration rate compared with large rivers, for example, as in comparing the Rio Grande River ($r^* = 2.6 \times 10^{-2}$) with the Mississippi River ($r^* = 8.1 \times 10^{-4}$) (Fig. 4a; Extended Data Table 2). The impact of channel curvature² on the observed difference in lateral migration rates across the studied rivers can be ruled out since r^* is calculated by averaging over multiple channel bends of similar sinuosity and curvature (Extended Data Figs. 4–6).

The distinction in normalized migration rates between the two groups of rivers further reveals controls on meander development and explains the cause of the order-of-magnitude uncertainty that is typical of empirical relations^{7,8}. We propose three drivers for lateral migration: the sediment supply, the discharge variability and the flooding intensity.

First, our study shows that, compared with the variable-sinuosity rivers, the high migration rate in the constant-sinuosity rivers is associated with a relatively high sediment supply, as evaluated using a sediment-to-water discharge ratio (that is, Q_s/Q_w ; Fig. 4b; Supplementary Information, Extended Data Table 2 and Extended Data Fig. 7). We postulate that the increased sediment supply, in particular, a sandy bed material load, enhances the deposition of point bars (that is, convex banks), thus promoting channel migration^{1,7,29}. Meanwhile, cut banks (that is, concave banks) that are constructed of sandy sediment are less cohesive and are therefore subject to retreat. Combined, point-bar advance and cut-bank retreat enhance the channel migration³⁰. In addition, local sediment input from alluvial valleys may promote lateral migration^{31,32}. For example, the Brazos and Trinity rivers are similar in terms of water discharge, flow depth and channel slope. However, the Holocene valley fills in the Brazos River are much sandier than those

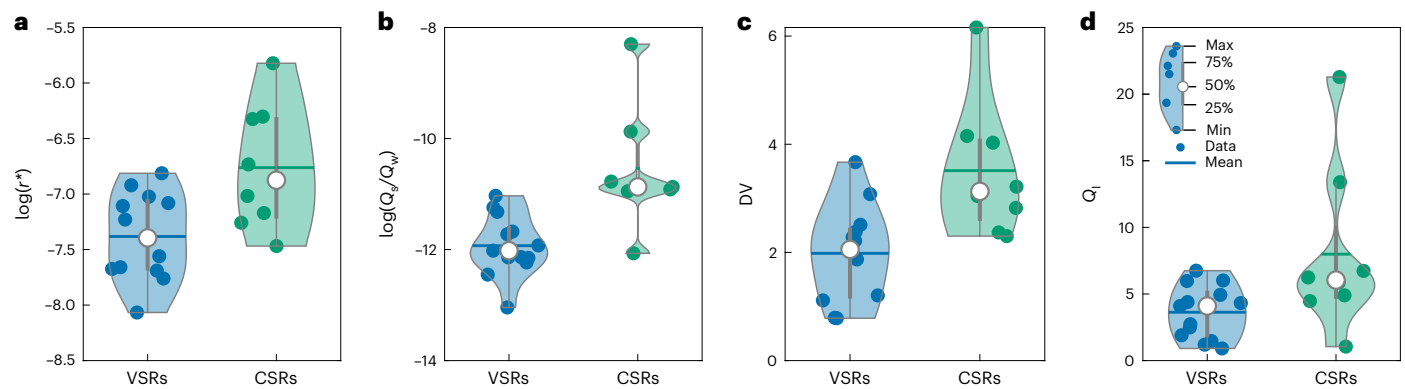


Fig. 4 | Channel migration rate, sediment supply and discharge properties for the investigated Earth rivers. a–d. Distributions and kernel densities of the normalized average channel migration rate r^* (a), the sediment-to-water discharge ratio (Q_s/Q_w) (b), the discharge variability (DV) (c) and the flood

intensity Q_i (d) (Supplementary Table 2). For each, the white circle marks the median, the filled circles denote individual rivers, the thick grey bar marks 25–70 percentile range and the horizontal line marks the mean. VSRs, variable-sinuosity rivers; CSRs, constant-sinuosity rivers.

in the Trinity River^{33–35}. Therefore, there are richer local sources of sandy bed material sediment making up banks and substrate in the Brazos River, so as to facilitate faster lateral channel migration than the Trinity River.

Second, the constant-sinuosity rivers possess a greater discharge variability (DV) compared with the variable-sinuosity rivers, where the DV is measured as the difference in average discharge from the dry to wet seasons (Fig. 4c; Methods). We suggest that a high DV, as one of the essential conditions for meander development^{36,37}, can result in disturbance of the equilibrium channel geometry and thus promote channel migration^{29,38,39}. Since the channel geometry (that is, the flow depth and width) is modified to accommodate bankfull discharge through lateral migration^{29,38,39}, a high DV is likely to induce frequent adjustment of the channel geometry through point-bar deposition and cut-bank erosion³⁸. For example, variable discharge will result in disequilibrium flow conditions that promote deposition on the channel bed¹⁸ and enhance the channel mobility⁴⁰.

Third, the constant-sinuosity rivers typically show average flood intensity (Q_i) values that are greater than those of the variable-sinuosity rivers, where Q_i measures the peakedness of the maximum daily discharge relative to the average discharge (Fig. 4d; Methods). Intensified discharge can result in overbank sediment transport, especially of fine-grain (cohesive) material to a distal floodplain^{41,42}. The transport of overbank sediment inhibits levee aggradation as overbank sedimentation is subdued⁴². The reduced deposition of cohesive material on the levee further promotes bank erosion as banks become less erosion-resistant³⁶. Therefore, channel migration rates increase because of weakened and denuded banks⁴¹.

Implications for understanding past and future rivers

We identify two spatial patterns of river channel sinuosity approaching the outlet: one where the average sinuosity increases drastically, and the other where the average sinuosity is relatively constant. This observation replaces the conventional view that lowland river sinuosity simply reduces downstream. The current findings provide insights for the challenging tasks of palaeohydrology and palaeoclimate^{3,9,19}. In the Martian examples, the variable-sinuosity rivers did not achieve a steady state, whereas the constant-sinuosity rivers did reach a steady state. These observations suggest that the two Martian river groups developed under low Q_s/Q_w , DV and Q_i conditions, and under high Q_s/Q_w , DV and Q_i conditions, respectively. This could be the result of different drainage basins²² and/or patterns, indicating local hydroclimates⁴³, despite the proximity of the studied Martian river systems, as well as

similarities in size. This is similar to the case of the Brazos and Trinity rivers, two systems that are less than one hundred kilometres apart but which possess starkly different planform properties and migration kinematics^{33–35}. Alternatively, the hydroclimate of the region could have shifted so that the two groups of Martian systems were developed under different flood regimes⁴⁴.

This information is useful for future models that evaluate different climate scenarios and runoff conditions on Mars⁴⁵. For example, hydrographs simulated using climate models can be used to predict the avulsion frequency and channel migration rate^{15,38}, which will determine the stage of sinuosity development as demonstrated in this study. The sinuosity of the Aeolis Dorsa channel systems indicates that both the avulsion timescale and the channel migration rate were subject to unique hydrographs. The simulated hydrographs using climate models can then be tested by comparing the modelled and observed channel sinuosity.

Finally, as Earth's climate warms, hydrological cycles and precipitation extremes are expected⁴⁶, leading to a higher variability in river discharge⁴⁷. Therefore, lowland rivers across the globe will shift into more constant-sinuosity rivers along with the risk of enhanced migration⁴⁸ and flooding⁴⁹, which will present a critical environmental and socio-economic challenge for adjacent human communities.

Online content

Any methods, additional references, Nature Portfolio reporting summaries, source data, extended data, supplementary information, acknowledgements, peer review information; details of author contributions and competing interests; and statements of data and code availability are available at <https://doi.org/10.1038/s41561-023-01231-1>.

References

- Ahmed, J., Constantine, J. A. & Dunne, T. The role of sediment supply in the adjustment of channel sinuosity across the Amazon Basin. *Geology* **47**, 807–810 (2019).
- Sylvester, Z., Durkin, P. & Covault, J. A. High curvatures drive river meandering. *Geology* **47**, 263–266 (2019).
- Kite, E. S. et al. Persistence of intense, climate-driven runoff late in Mars history. *Sci. Adv.* **5**, eaav7710 (2019).
- Leopold, L. B. & Wolman, M. G. *River Channel Patterns: Braided, Meandering, and Straight* Professional Paper 282-B (US Geological Survey, 1957); <https://pubs.er.usgs.gov/publication/pp282B>
- Wilkerson, G. V. & Parker, G. Physical basis for quasi-universal relationships describing bankfull hydraulic geometry of sand-bed rivers. *J. Hydraul. Eng.* **137**, 739–753 (2011).

6. Wiman, C., Hamilton, B., Dee, S. G. & Muñoz, S. E. Reduced lower Mississippi River discharge during the Medieval era. *Geophys. Res. Lett.* **48**, e2020GL091182 (2021).
7. Constantine, J. A., Dunne, T., Ahmed, J., Legleiter, C. & Lazarus, E. D. Sediment supply as a driver of river meandering and floodplain evolution in the Amazon Basin. *Nat. Geosci.* **7**, 899–903 (2014).
8. Ielpi, A. & Lapôtre, M. G. A. A tenfold slowdown in river meander migration driven by plant life. *Nat. Geosci.* **13**, 82–86 (2020).
9. Hayden, A. T., Lamb, M. P. & McElroy, B. J. Constraining the timespan of fluvial activity from the intermittency of sediment transport on Earth and Mars. *Geophys. Res. Lett.* **48**, e2021GL092598 (2021).
10. Lapôtre, M. G. A. & Ielpi, A. The pace of fluvial meanders on Mars and implications for the western delta deposits of Jezero crater. *AGU Adv.* **1**, e2019AV000141 (2020).
11. Ikeda, H. in *River Meandering* Vol. 12 (eds Ikeda, S. & Parker, G.) 51–68 (American Geophysical Union, 1989); <https://doi.org/10.1029/WM012p0051>
12. Hudson, P. F. & Kesel, R. H. Channel migration and meander-bend curvature in the lower Mississippi River prior to major human modification. *Geology* **28**, 531–534 (2000).
13. Cardenas, B. T., Mohrig, D. & Goudge, T. A. Fluvial stratigraphy of valley fills at Aeolis Dorsa, Mars: evidence for base-level fluctuations controlled by a downstream water body. *Geol. Soc. Am. Bull.* **130**, 484–498 (2018).
14. DiBiase, R. A., Limaye, A. B., Scheingross, J. S., Fischer, W. W. & Lamb, M. P. Deltaic deposits at Aeolis Dorsa: sedimentary evidence for a standing body of water on the northern plains of Mars. *J. Geophys. Res. Planets* **118**, 1285–1302 (2013).
15. Chadwick, A. J., Lamb, M. P. & Ganti, V. Accelerated river avulsion frequency on lowland deltas due to sea-level rise. *Proc. Natl Acad. Sci. USA* **117**, 17584–17590 (2020).
16. Chatanantavet, P., Lamb, M. P. & Nittrouer, J. A. Backwater controls of avulsion location on deltas. *Geophys. Res. Lett.* <https://doi.org/10.1029/2011GL050197> (2012).
17. Ganti, V., Chadwick, A. J., Hassenruck-Gudipati, H. J. & Lamb, M. P. Avulsion cycles and their stratigraphic signature on an experimental backwater-controlled delta: backwater-controlled avulsion cycles. *J. Geophys. Res. Earth Surf.* **121**, 1651–1675 (2016).
18. Ganti, V., Chadwick, A. J., Hassenruck-Gudipati, H. J., Fuller, B. M. & Lamb, M. P. Experimental river delta size set by multiple floods and backwater hydrodynamics. *Sci. Adv.* **2**, e1501768 (2016).
19. Hayden, A. T. & Lamb, M. P. Fluvial sinuous ridges of the Morrison Formation, USA: meandering, scarp retreat, and implications for Mars. *J. Geophys. Res. Planets* **125**, e2020JE006470 (2020).
20. Hayden, A. T., Lamb, M. P. & Carney, A. J. Similar curvature-to-width ratios for channels and channel belts: implications for paleo-hydraulics of fluvial ridges on Mars. *Geology* <https://doi.org/10.1130/G48370.1> (2021).
21. Cardenas, B. T., Lamb, M. P., Jobe, Z. R., Mohrig, D. & Swartz, J. M. Morphodynamic preservation of fluvial channel belts. *Sediment. Rec.* <https://doi.org/10.2110/001c.66285> (2023).
22. Cardenas, B. T. & Lamb, M. P. Paleogeographic reconstructions of an ocean margin on Mars based on deltaic sedimentology at Aeolis Dorsa. *J. Geophys. Res. Planets* **127**, e2022JE007390 (2022).
23. Chadwick, A. J., Lamb, M. P., Moodie, A. J., Parker, G. & Nittrouer, J. A. Origin of a preferential avulsion node on lowland river deltas. *Geophys. Res. Lett.* **46**, 4267–4277 (2019).
24. Prasojo, O. A., Hoey, T. B., Owen, A. & Williams, R. D. Slope break and avulsion locations scale consistently in global deltas. *Geophys. Res. Lett.* **49**, e2021GL093656 (2022).
25. Ratliff, K. M., Hutton, E. W. H. & Murray, A. B. Modeling long-term delta dynamics reveals persistent geometric river avulsion locations. *Earth Planet. Sci. Lett.* **559**, 116786 (2021).
26. Bogoni, M., Putti, M. & Lanzoni, S. Modeling meander morphodynamics over self-formed heterogeneous floodplains. *Water Resour. Res.* **53**, 5137–5157 (2017).
27. Constantine, J. A., McLean, S. R. & Dunne, T. A mechanism of chute cutoff along large meandering rivers with uniform floodplain topography. *Geol. Soc. Am. Bull.* **122**, 855–869 (2010).
28. Jarriel, T., Swartz, J. & Passalacqua, P. Global rates and patterns of channel migration in river deltas. *Proc. Natl Acad. Sci. USA* **118**, e2103178118 (2021).
29. Eke, E., Parker, G. & Shimizu, Y. Numerical modeling of erosional and depositional bank processes in migrating river bends with self-formed width: morphodynamics of bar push and bank pull. *J. Geophys. Res. Earth Surf.* **119**, 1455–1483 (2014).
30. van de Lageweg, W. I., van Dijk, W. M., Baar, A. W., Rutten, J. & Kleinhans, M. G. Bank pull or bar push: what drives scroll-bar formation in meandering rivers? *Geology* **42**, 319–322 (2014).
31. Wu, C. et al. Lateral migration dynamics and bank erodibility of the lowermost Mississippi River. In *Proc. AGU Fall Meeting EP52A-05* (American Geophysical Union, 2022).
32. Dong, T. Y. et al. Roles of bank material in setting bankfull hydraulic geometry as informed by the Selenga River delta, Russia. *Water Resour. Res.* **55**, 827–846 (2019).
33. Anderson, J. B. et al. Recycling sediments between source and sink during a eustatic cycle: systems of late Quaternary northwestern Gulf of Mexico Basin. *Earth Sci. Rev.* **153**, 111–138 (2016).
34. Simms, A. R., Anderson, J. B., Taha, Z. P. & Rodriguez, A. B. in *Incised Valleys in Time and Space* Vol. 85 (eds Dalrymple, R. W. et al.) (SEPM Society for Sedimentary Geology, 2006); <https://doi.org/10.2110/pec.06.85.0117>
35. Guerit, L., Foreman, B. Z., Chen, C., Paola, C. & Castelltort, S. Autogenic delta progradation during sea-level rise within incised valleys. *Geology* **49**, 273–277 (2020).
36. van Dijk, W. M., van de Lageweg, W. I. & Kleinhans, M. G. Formation of a cohesive floodplain in a dynamic experimental meandering river. *Earth Surf. Process. Landf.* **38**, 1550–1565 (2013).
37. van Dijk, W. M., van de Lageweg, W. I. & Kleinhans, M. G. Experimental meandering river with chute cutoffs. *J. Geophys. Res. Earth Surf.* <https://doi.org/10.1029/2011JF002314> (2012).
38. Naito, K. & Parker, G. Can bankfull discharge and bankfull channel characteristics of an alluvial meandering river be cospecified from a flow duration curve? *J. Geophys. Res. Earth Surf.* **124**, 2381–2401 (2019).
39. Parker, G. et al. A new framework for modeling the migration of meandering rivers. *Earth Surf. Process. Landf.* **36**, 70–86 (2011).
40. Nittrouer, J. A., Shaw, J., Lamb, M. P. & Mohrig, D. Spatial and temporal trends for water-flow velocity and bed-material sediment transport in the lower Mississippi River. *Geol. Soc. Am. Bull.* **124**, 400–414 (2012).
41. Barefoot, E. A., Nittrouer, J. A. & Straub, K. M. Non-monotonic floodplain responses to changes in flooding intensity. *J. Geophys. Res. Earth Surf.* **126**, e2021JF006310 (2021).
42. Han, J. & Kim, W. Linking levee-building processes with channel avulsion: geomorphic analysis for assessing avulsion frequency and channel reoccupation. *Earth Surf. Dynam.* **10**, 743–759 (2022).
43. Syvitski, J. P. M. & Milliman, J. D. Geology, geography, and humans battle for dominance over the delivery of fluvial sediment to the coastal ocean. *J. Geol.* **115**, 1–19 (2007).
44. Hansford, M. R., Plink-Björklund, P. & Jones, E. R. Global quantitative analyses of river discharge variability and hydrograph shape with respect to climate types. *Earth Sci. Rev.* **200**, 102977 (2020).
45. Stucky de Quay, G., Goudge, T. A., Kite, E. S., Fassett, C. I. & Guzewich, S. D. Limits on runoff episode duration for early Mars: integrating lake hydrology and climate models. *Geophys. Res. Lett.* **48**, e2021GL093523 (2021).

46. Donat, M. G., Lowry, A. L., Alexander, L. V., O’Gorman, P. A. & Maher, N. More extreme precipitation in the world’s dry and wet regions. *Nat. Clim. Chang.* **6**, 508–513 (2016).
47. Bouwer, L. M., Vermaat, J. E. & Aerts, J. C. J. H. Regional sensitivities of mean and peak river discharge to climate variability in Europe. *J. Geophys. Res. Atmos.* <https://doi.org/10.1029/2008JD010301> (2008).
48. Barefoot, E. A. et al. Evidence for enhanced fluvial channel mobility and fine sediment export due to precipitation seasonality during the Paleocene–Eocene thermal maximum. *Geology* <https://doi.org/10.1130/G49149.1> (2021).
49. Nanditha, J. S. et al. The Pakistan flood of August 2022: causes and implications. *Earths Future* **11**, e2022EF003230 (2023).

Publisher’s note Springer Nature remains neutral with regard to jurisdictional claims in published maps and institutional affiliations.

Springer Nature or its licensor (e.g. a society or other partner) holds exclusive rights to this article under a publishing agreement with the author(s) or other rightsholder(s); author self-archiving of the accepted manuscript version of this article is solely governed by the terms of such publishing agreement and applicable law.

© The Author(s), under exclusive licence to Springer Nature Limited 2023

Methods

The avulsion length was calculated as the river distance from the avulsion node to the downstream outlet for the Apalachicola, Suwannee, Sabine, Neches, Don, Yana, Kobuk and Mackenzie rivers. The avulsion node was identified using satellite images or a digital elevation model. For the rest of the rivers analysed in this study, the avulsion length was approximated using the backwater length. The upstream extent of the backwater influence can be approximated using a ratio of the reach-averaged bankfull flow depth (h) and the channel bed slope (S) as a backwater length (L_b) scale⁵⁰:

$$L_b = h/S. \quad (1)$$

For the Martian river systems, avulsion length was calculated as the projected distance of the avulsion node to the downstream distal reach of the fluvial sandstone ridge.

Channel centrelines were traced mainly from recent satellite images to calculate the sinuosity. For rivers where the channel paths had been modified through straightening, the channel centrelines were traced from historical maps that were dated before the engineering modification (Supplementary Information). The sinuosity was calculated for each meander bend, where a meander bend is bounded at the upstream and downstream ends of inflection points on the channel centreline, where the curvature is zero. Sinuosity values were calculated from the ratio between the streamwise distance and the Cartesian distance between two adjacent inflection points.

A numerical model was used to explore the temporal variability in the channel sinuosity. We used the model of Ikeda et al.⁵¹ with the numerical implementation method of Sun and co-workers⁵². Our model simulates channel migration through bank erosion caused by an excess flow velocity near the cut bank:

$$\zeta = Eu_b, \quad (2)$$

where ζ is the lateral migration rate, E is the erosional coefficient and u_b is the excess flow velocity near bank. The excess flow velocity u_b can be calculated using

$$u_0 \frac{\partial u_b}{\partial s} + 2 \frac{u_0}{h} C_f u_b = b \left[-u_0^2 \frac{\partial \xi}{\partial s} + C_f \xi \left(\frac{u_0^4}{gh^2} + A \frac{u_0^2}{h} \right) \right], \quad (3)$$

where u_0 is the reach-averaged flow velocity, s is the streamwise distance, b is the reach-averaged half-bankfull flow width, C_f is the friction coefficient, ξ is the local curvature of channel centreline, g is the gravitational acceleration and A is the constant slope factor. Meander neck cutoff is triggered when the Cartesian distance between any two points along the river path becomes less than a given channel width. The erosional coefficient for natural systems was calibrated by matching the actual and modelled channel migration rates (Supplementary Information).

The average channel migration rate (r) and the normalized channel migration rate (r^*) are defined as:

$$r = \frac{\alpha}{lN}, \quad (4)$$

$$r^* = \frac{r}{B(1 - P_{bf})}, \quad (5)$$

where α is the area of the polygons enclosed by two channel courses from succeeding time periods, l is the length of the channel course, N is the number of years separating the two river courses, B is the bankfull channel width, P_{bf} is the cumulative frequency of bankfull discharge and $(1 - P_{bf})$ denotes the exceedance probability of bankfull discharge. The P_{bf} term is introduced assuming that river migration is only active

when discharge meets or exceeds bankfull discharge³⁸.

The discharge variability DV compares the difference between the wettest and driest months on record⁴⁴:

$$DV = \frac{Q_{w-max} - Q_{w-min}}{\bar{Q}_w}, \quad (6)$$

where Q_{w-max} and Q_{w-min} are, respectively, the wettest and driest monthly average discharges on record and \bar{Q}_w is the average discharge.

The flood intensity Q_i in this study was measured as the magnitude of the peak daily discharge relative to the average discharge:

$$Q_i = \frac{\sum_1^n \frac{Q_{max}^i - Q_{min}^i}{Q_w}}{m}, \quad (7)$$

where m is the number of years of daily discharge record, Q_{max}^i and Q_{min}^i are the maximum and minimum average daily discharges each for the i th year on record, respectively. We used daily discharge records dated before major dam constructions to calculate DV and Q_i for the two groups of Earth rivers.

Data availability

The compiled data on river paths for analysis of the sinuosity and lateral migration rate are available via Figshare at <https://doi.org/10.6084/m9.figshare.22308637>.

Code availability

The MATLAB codes for plotting Figs. 2–4 are available for download from <https://doi.org/10.5281/zenodo.7749850>.

References

- Paola, C. & Mohrig, D. Palaeohydraulics revisited: palaeoslope estimation in coarse-grained braided rivers. *Basin Res.* **8**, 243–254 (1996).
- Ikeda, S., Parker, G. & Sawai, K. Bend theory of river meanders. Part 1. Linear development. *J. Fluid Mech.* **112**, 363–377 (1981).
- Sun, T., Meakin, P., Jøssang, T. & Schwarz, K. A simulation model for meandering rivers. *Water Resour. Res.* **32**, 2937–2954 (1996).
- Larsen, E. W. *Mechanics and Modeling of River Meander Migration*. PhD thesis, Univ. California, Berkeley (1995).
- Moran, K. E., Nittroer, J. A., Perillo, M. M., Lorenzo-Trueba, J. & Anderson, J. B. Morphodynamic modeling of fluvial channel fill and avulsion time scales during early Holocene transgression, as substantiated by the incised valley stratigraphy of the Trinity River, Texas. *J. Geophys. Res. Earth Surf.* **122**, 215–234 (2017).
- Hobo, N., Makaske, B., Wallinga, J. & Middelkoop, H. Reconstruction of eroded and deposited sediment volumes of the embanked River Waal, the Netherlands, for the period AD 1631–present. *Earth Surf. Process. Landf.* **39**, 1301–1318 (2014).
- Woolderink, H. A. G., Cohen, K. M., Kasse, C., Kleinhans, M. G. & Van Balen, R. T. Patterns in river channel sinuosity of the Meuse, Roer and Rhine rivers in the Lower Rhine Embayment rift-system, are they tectonically forced? *Geomorphology* **375**, 107550 (2021).
- Gensen, M. R. A., Warmink, J. J., Huthoff, F. & Hulscher, S. J. M. H. Feedback mechanism in bifurcating river systems: the effect on water-level sensitivity. *Water* **12**, 1915 (2020).
- Pol, J. *Hydrograph Shape Variability on the River Meuse*. MSc thesis, Delft Univ. Technology (2014).
- Berendsen, H. J. A. & Stouthamer, E. Paleogeographic evolution and avulsion history of the Holocene Rhine–Meuse delta, The Netherlands. *Neth. J. Geosci.* **81**, 97–112 (2002).
- Berendsen, H. J. A. & Stouthamer, E. Late Weichselian and Holocene palaeogeography of the Rhine–Meuse delta, The Netherlands. *Palaeogeogr. Palaeoclimatol. Palaeoecol.* **161**, 311–335 (2000).

61. Giosan, L. et al. Young Danube delta documents stable Black Sea level since the middle Holocene: morphodynamic, paleogeographic, and archaeological implications. *Geology* **34**, 757–760 (2006).
62. Fisk, H. N. *Geological Investigation of the Alluvial Valley of the Lower Mississippi River* (Mississippi River Commission, US Army Corps of Engineers, 1944).
63. Chamberlain, E. L., Törnqvist, T. E., Shen, Z., Mauz, B. & Wallinga, J. Anatomy of Mississippi Delta growth and its implications for coastal restoration. *Sci. Adv.* **4**, eaar4740 (2018).
64. Heitmuller, F. T. Channel adjustments to historical disturbances along the lower Brazos and Sabine Rivers, south-central USA. *Geomorphology* **204**, 382–398 (2014).
65. Strom, K. & Rouhnia, M. *Suspended Sediment Sampling and Annual Sediment Yield on the Lower Brazos River* (Texas Water Development Board, 2013); https://www.twdb.texas.gov/publications/reports/contracted_reports/doc/1000011085_1100011340_brazossediment.pdf
66. Swartz, J. M., Goudge, T. A. & Mohrig, D. C. Quantifying coastal fluvial morphodynamics over the last 100 years on the lower Rio Grande, USA and Mexico. *J. Geophys. Res. Earth Surf.* **125**, e2019JF005443 (2020).
67. Ijaz, M. W., Mahar, R. B., Ansari, K., Siyal, A. A. & Anjum, M. N. Integrated assessment of contemporary hydro-geomorphologic evolution of the Indus River Estuary, Pakistan in context to regulated fluvial regimes. *Estuar. Coast. Shelf Sci.* **236**, 106657 (2020).
68. Syvitski, J. P. M. et al. Anthropocene metamorphosis of the Indus Delta and lower floodplain. *Anthropocene* **3**, 24–35 (2013).
69. Park, E., Lim, J., Ho, H. L., Herrin, J. & Chitwatkulisiri, D. Source-to-sink sediment fluxes and budget in the Chao Phraya River, Thailand: a multi-scale analysis based on the national dataset. *J. Hydrol.* **594**, 125643 (2021).
70. Tingsanchali, T. & Kumar Lal, N. Subsidence of flood waves in overbank flow areas. *J. Hydraul. Res.* **26**, 585–597 (1988).
71. Tanabe, S. et al. Stratigraphy and Holocene evolution of the mud-dominated Chao Phraya delta, Thailand. *Quat. Sci. Rev.* **22**, 789–807 (2003).
72. Meade, R. H. & Moody, J. A. Causes for the decline of suspended-sediment discharge in the Mississippi River system, 1940–2007. *Hydrol. Process.* **24**, 35–49 (2010).
73. Garvin, M. G. *Late Quaternary Geochronologic, Stratigraphic, and Sedimentologic Framework of the Trinity River Incised Valley: East Texas Coast*. MSc thesis, Louisiana State Univ. (2008).
74. Erkens, G., Cohen, K. M., Gouw, M. J. P., Middelkoop, H. & Hoek, W. Z. in *Sediment Dynamics and the Hydromorphology of Fluvial Systems* (eds Rowan, J. S. et al.) IAHS Publication Number 306; 406–415 (International Association of Hydrological Sciences, 2006).
75. Toonen, W. H. J. Flood frequency analysis and discussion of non-stationarity of the Lower Rhine flooding regime (AD 1350–2011): using discharge data, water level measurements, and historical records. *J. Hydrol.* **528**, 490–502 (2015).
76. Panin, N. & Jipa, D. Danube river sediment input and its interaction with the north-western Black Sea. *Estuar. Coast. Shelf Sci.* **54**, 551–562 (2002).
77. Cox, J. R. et al. Anthropogenic effects on the contemporary sediment budget of the lower Rhine–Meuse Delta channel network. *Earths Future* **9**, e2020EF001869 (2021).
78. Garzanti, E., Andò, S., Padoan, M., Vezzoli, G. & El Kammar, A. The modern Nile sediment system: processes and products. *Quat. Sci. Rev.* **130**, 9–56 (2015).
79. Wohl, E. E. in *Large Rivers: Geomorphology and Management* (ed. Gupta, A.) 29–44 (Wiley, 2007); <https://doi.org/10.1002/9780470723722.ch3>
80. Milliman, J. D. & Syvitski, J. P. M. Geomorphic/tectonic control of sediment discharge to the ocean: the importance of small mountainous rivers. *J. Geol.* **100**, 525–544 (1992).
81. Heitmuller, F. T. & Greene, L. E. *Historical Channel Adjustment and Estimates of Selected Hydraulic Values in the Lower Sabine River and Lower Brazos River Basins, Texas and Louisiana*. Scientific Investigations Report 2009-5174 (US Geological Survey, 2009); <https://pubs.er.usgs.gov/publication/sir20095174>
82. Inam, A. et al. in *Large Rivers: Geomorphology and Management* (ed. Gupta, A.) 333–346 (Wiley, 2007); <https://doi.org/10.1002/9780470723722.ch16>

Acknowledgements

Funding for this project was provided by the National Research Foundation of Korea (NRF-2017R1A6A1A07015374) to W.K., Yonsei University (Post-Doctoral Researcher Supporting Program, Yonsei University Research Fund #2021-12-0018) to C.W. and the Excellent Young Scientist Fund (Overseas, 2021) from NSFC to H.M.

Author contributions

C.W. and W.K. conceived the paper. C.W., B.T.C., R.H. and A.M. collected the data. All authors contributed to the analysis, writing, reviewing and editing.

Competing interests

The authors declare no competing interests.

Additional information

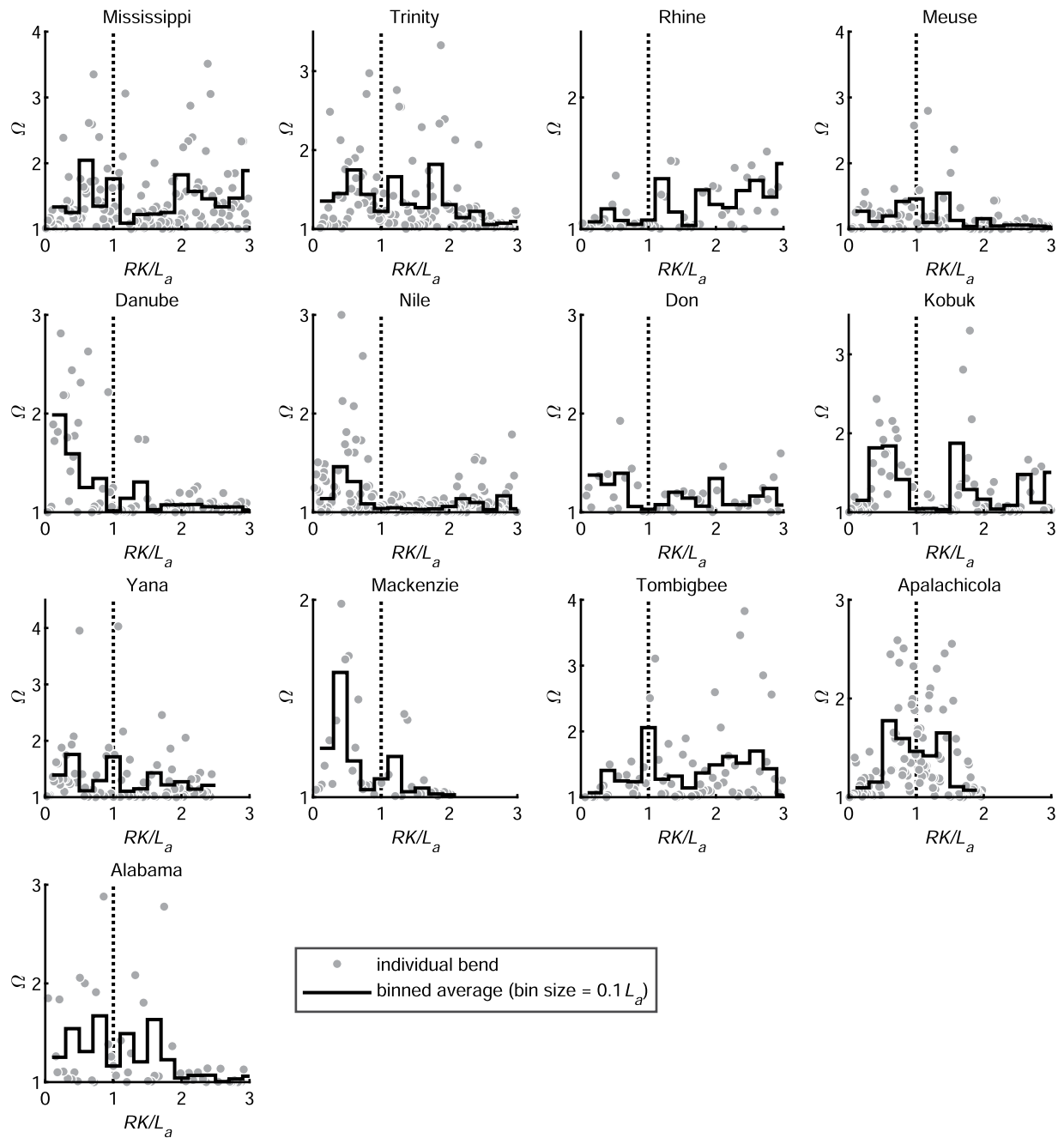
Extended data is available for this paper at <https://doi.org/10.1038/s41561-023-01231-1>.

Supplementary information The online version contains supplementary material available at <https://doi.org/10.1038/s41561-023-01231-1>.

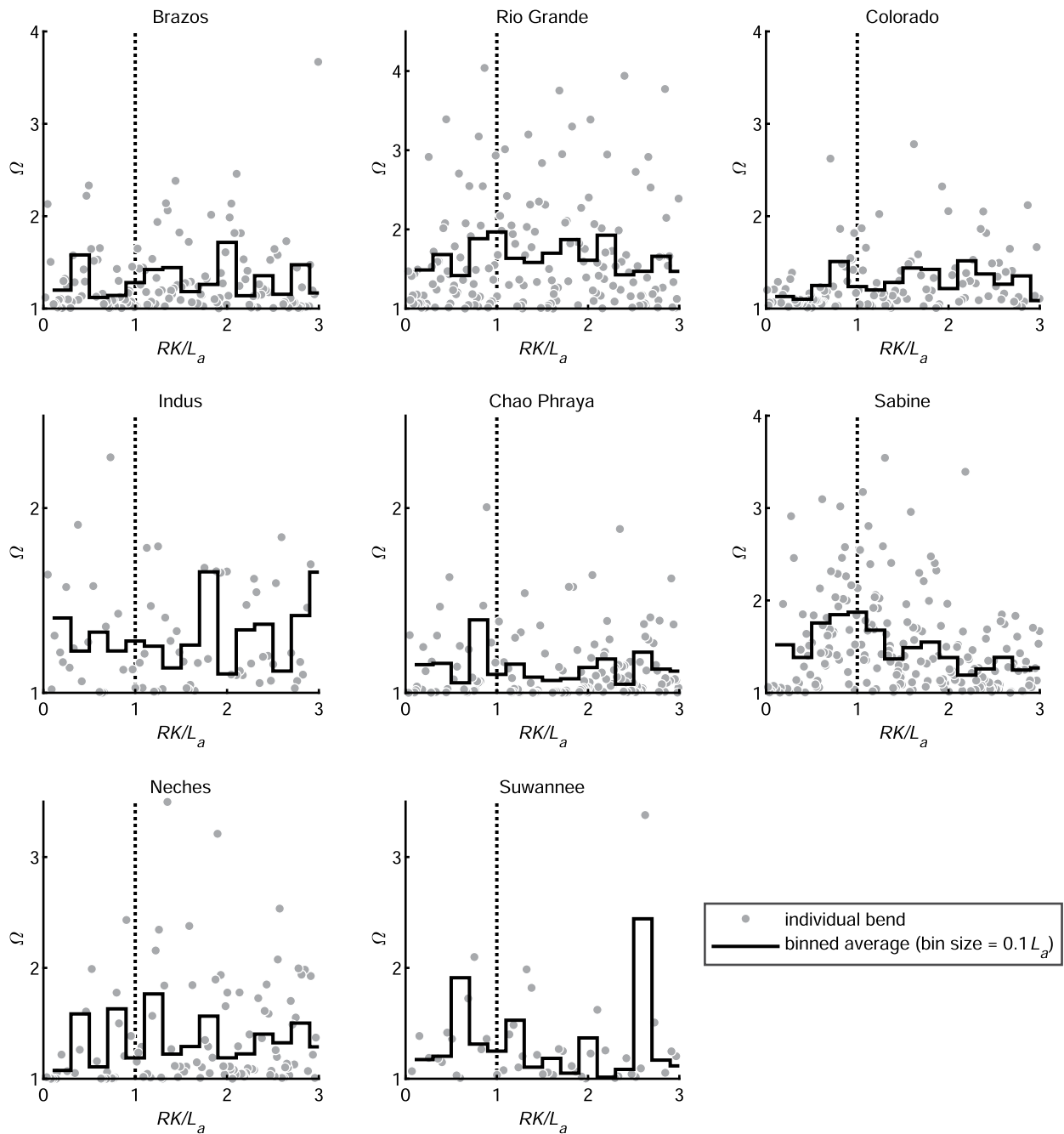
Correspondence and requests for materials should be addressed to Wonsuck Kim.

Peer review information *Nature Geoscience* thanks Joshua Ahmed and the other, anonymous, reviewer(s) for their contribution to the peer review of this work. Primary Handling Editor: Tamara Goldin, in collaboration with the *Nature Geoscience* team.

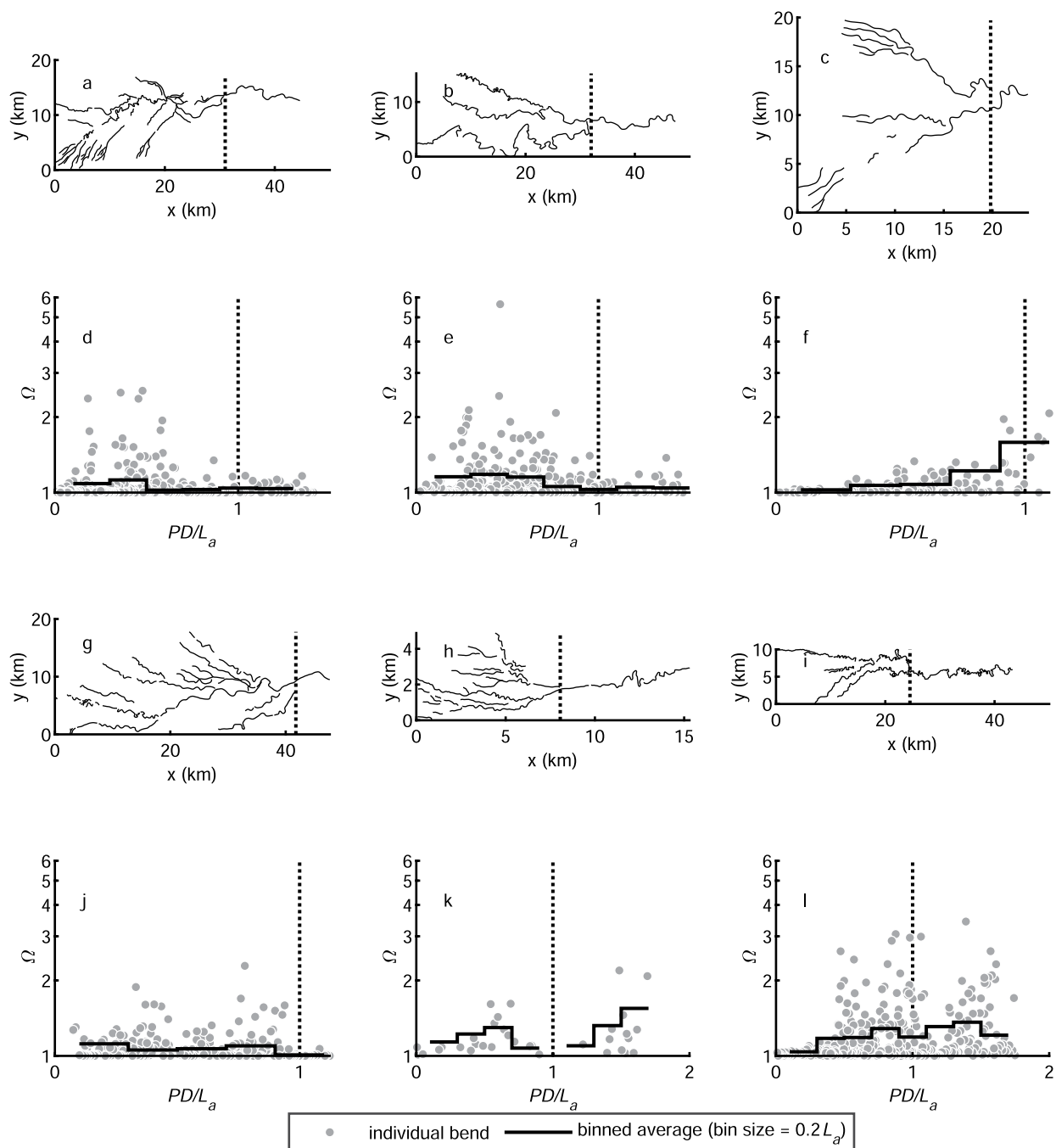
Reprints and permissions information is available at www.nature.com/reprints.



Extended Data Fig. 1 | Spatial trend in channel sinuosity Ω of variable-sinuosity Earth rivers. Dots are sinuosity measurements of individual bends and the black solid lines are binned averages with a bin size of $0.1L_a$, where L_a is the avulsion length.

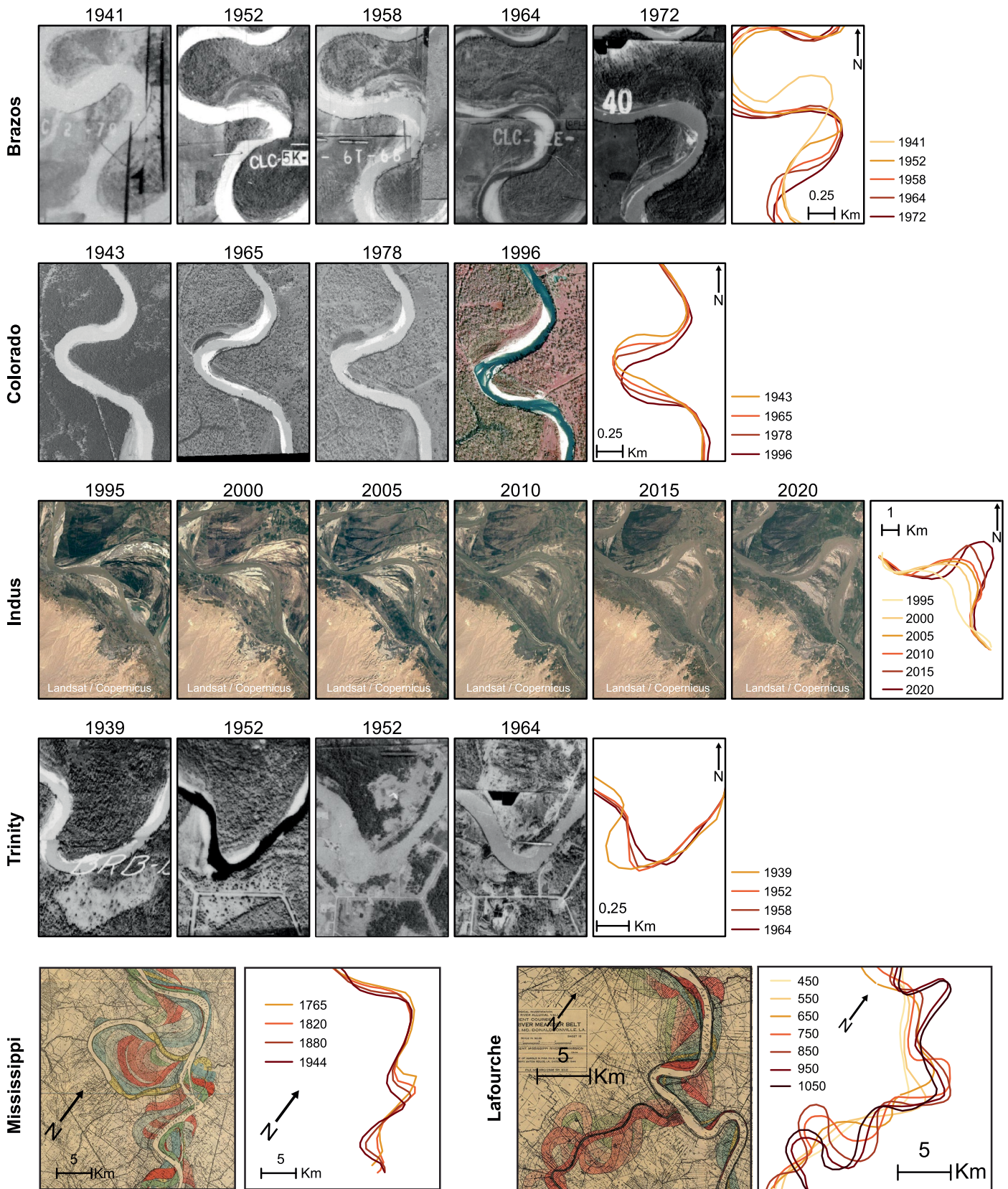


Extended Data Fig. 2 | Spatial trend in channel sinuosity Ω of constant-sinuosity Earth rivers. Dots are sinuosity measurements of individual bends and the black solid lines are binned averages with a bin size of $0.1L_a$, where L_a is the avulsion length.

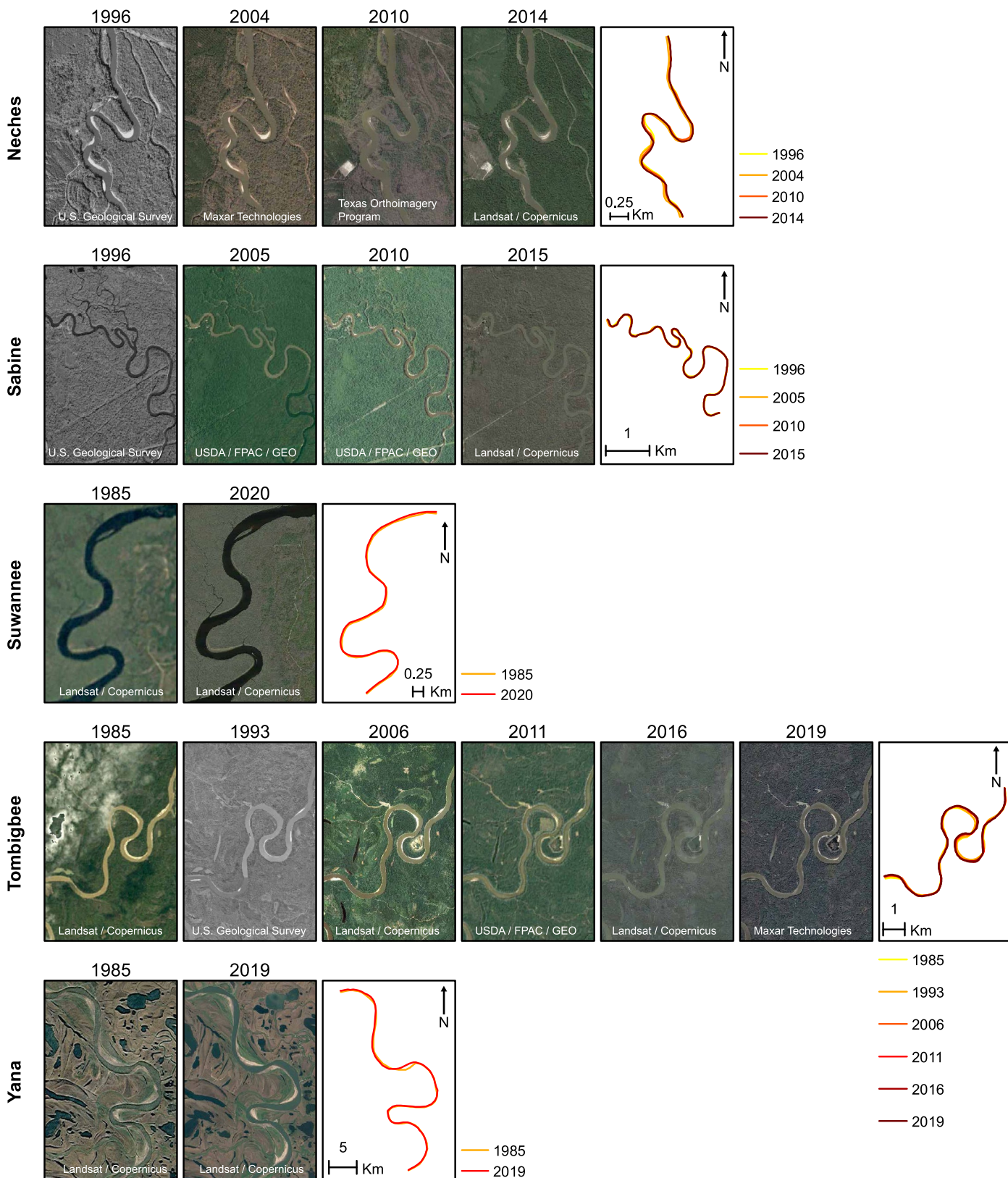


Extended Data Fig. 3 | Planform patterns of fluvial sandstone ridges of 6 Martian fluvial-deltaic systems (a-c and g-i) and their associated spatial trends in sinuosity Ω (d-f and j-l). Dots are sinuosity measurements of individual bends and the black solid lines are binned averages with a bin size of $0.1L_a$, where

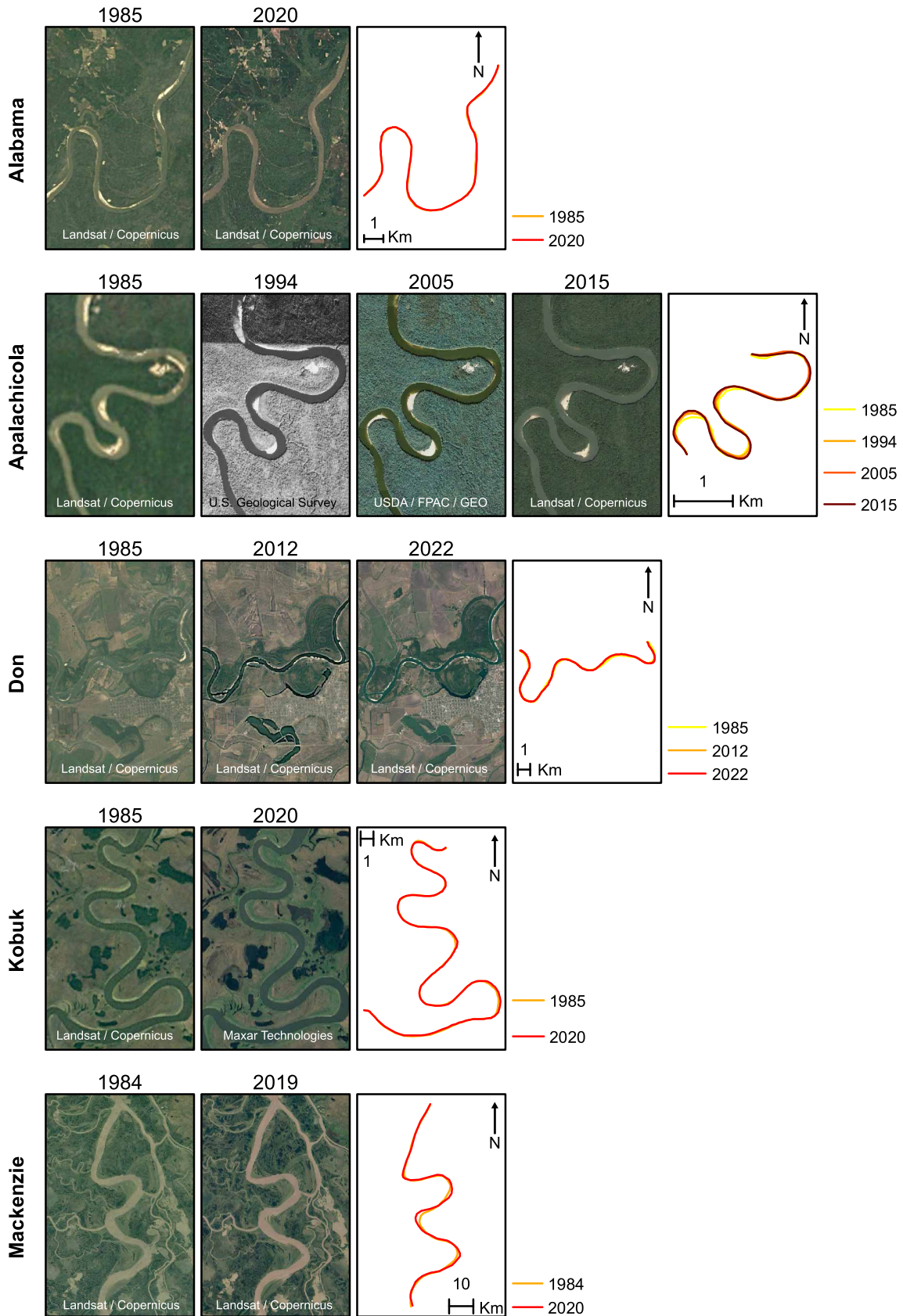
L_a is the avulsion length each marked by a dashed line. Projected distance PD of sinuosity measurements is normalized by L_a . Dashed line marks the avulsion location.



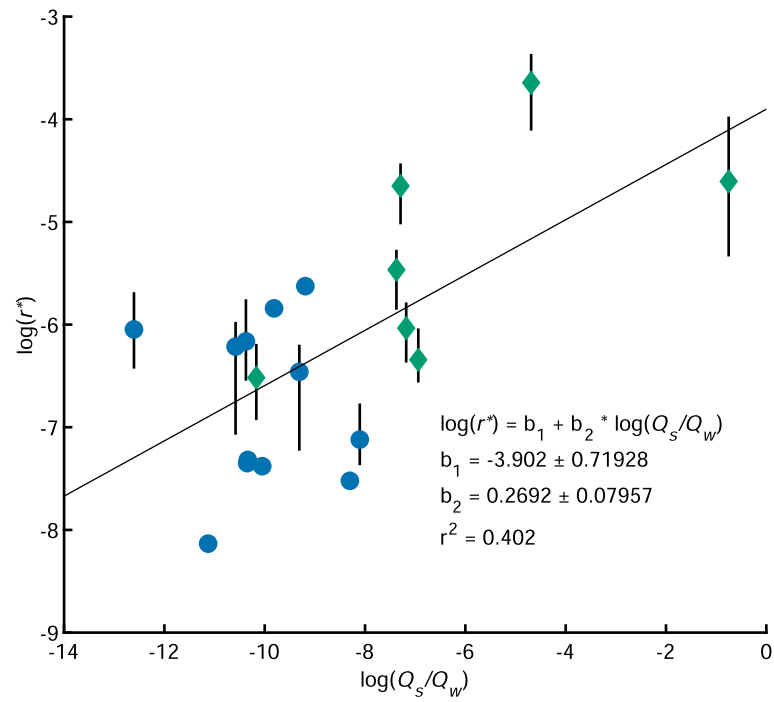
Extended Data Fig. 4 | Historical images, maps and satellite images of the Brazos, Colorado, Indus, Trinity, and Mississippi rivers. River centerlines were traced to calculate lateral channel migration rates. Credit: Brazos, Colorado and Trinity, Texas Natural Resources Information System; Indus, Landsat Copernicus via Google Earth; Mississippi and Lafourche, US Army Corps of Engineers.



Extended Data Fig. 5 | Satellite images and associated river centerlines for the Neches, Sabine, Suwannee, Tombigbee, and Yana rivers. Credit: Google Earth (third-party data providers are listed on the image).



Extended Data Fig. 6 | Satellite images and associated river centerlines for the Alabama, Apalachicola, Don, Kobuk, and Mackenzie rivers. Credit: Google Earth (third-party data providers are listed on the image).



Extended Data Fig. 7 | Correlation between sediment supply and channel lateral migration rate. Blue dots and green diamonds represent the average measured lateral migration rate for variable- and constant-sinuosity river groups, respectively. Error bar denotes the measured maximum and minimum lateral

migration rate for the natural rivers. The black line represents the regression fit. Sample size for each data point corresponds to the number of migration rate measurements based on traced centerlines at different times (Extended Data Figs. 4–6).

Extended Data Table 1 | Key model input parameters^{53–71} for natural rivers in Fig. 3

	h (m)	B (m)	u_0 (m/s)	C_f	E_{cali}	t_a (year)	<i>sources</i>
Mississippi	20	1300	2	0.005	9.53E-07	1000	40,53
Trinity	5	200	1.46	0.005	4.72E-07	934	54
Rhine	7.3	425	1.4	0.005	8.50E-07	1000	55–57
Meuse	5	150	1.67	0.005	9.70E-08	1760	56,58–60
Danube	6.3	1250	1.23	0.005	5.93E-07	1570	61
Nile	/	/	/	/	/	/	
Lafourche	20	1300	2	0.005	9.53E-07	750	62,63
Brazos	7.7	153	1.27	0.005	1.60E-06	2500	64,65
Rio Grande	5	100	1.4	0.005	3.55E-06	1000	66
Colorado	3.3	100	1.11	0.005	7.66E-07	2500	
Indus	8	500	0.72	0.005	2.88E-06	1000	67,68
Chao Phraya	6.77	251	1.19	0.005	1.44E-06	2000	69–71

Extended Data Table 2 | Sediment (Q_s) and water budget (Q_w), discharge variability (DV), flood intensity (Q_I), and lateral migration rate (r^*) for natural rivers^{72–82}

	Q_s (ton/year)	Q_w (m ³ /s)	Q_s/Q_w	DV	Q_I	r^*	references
Mississippi	4.00E+08	15855	3.02E-04	1.47	1.98	8.09E-04	72
Trinity	5.52E+06	730	9.05E-05	6.02	9.17	1.56E-03	73
Rhine	4.25E+06	2000	2.54E-05	2.49	3.01	2.00E-03	74,75
Danube	5.17E+07	6047	1.02E-04	4.32	4.67	3.60E-03	76
Meuse	1.18E+06	327	4.32E-05	1.2	1.96	6.24E-04	77
Nile	2.30E+08	2810	9.79E-04	0.91	/	/	78,79
Don	7.70E+05	624.86	1.47E-05	1.9	6.28	2.93E-04	80
Kobuk	/	/	2.48E-04	5.97	5.54	5.41E-04	
Yana	3.00E+06	1107.92	3.24E-05	6.75	5.95	6.63E-04	80
Mackenzie	4.20E+07	9180	5.47E-05	2.73	2.78	2.90E-03	80
Tombigbee	2.20E+06	844.05	3.12E-05	4.93	5.71	2.11E-03	80
Apalachicola	1.70E+05	607.61	3.35E-06	4.1	7.69	2.37E-03	80
Alabama	2.30E+06	858.94	3.20E-05	4.39	4.74	6.43E-04	80
Brazos	1.24E+07	218	6.81E-04	6.24	10.07	9.57E-03	33,81
Rio Grande	3.69E+07	48	9.20E-03	5.85	5.75	2.61E-02	33,66
Colorado	4.91E+06	77	7.62E-04	21.28	10.38	2.39E-03	33
Indus	8.50E+10	2156	4.72E-01	6.73	15.4	1.00E-02	82
Chao Phraya	2.53E+07	483	6.27E-04	4.47	5.92	4.23E-03	69
Sabine	7.50E+05	234	3.84E-05	4.9	7.61	1.48E-03	80
Neches	1.33E+06	16.4	9.70E-04	1.05	7.06	1.76E-03	80
Suwannee	/	/	/	13.39	8.04	9.71E-04	

Note: sediment budget data is collected from previous literatures listed in the reference column (SI). Water discharge Q_w is calculated as the average discharge from the hydrographs. Discharge variability (DV) and flood intensity (Q_I) are calculated from daily discharge (Methods). Lateral migration rate (r^*) is calculated using historical channel paths (Methods).